

Microstructural Analysis of Orientation-Dependent Recovery and Recrystallization in a Modified 9Cr-1Mo Steel Deformed by Compression at a High Strain Rate



ZHENBO ZHANG, YUBIN ZHANG, OLEG V. MISHIN, NAIRONG TAO, WOLFGANG PANTLEON, and DORTE JUUL JENSEN

The evolution of the microstructure and texture during annealing of a modified ferritic/martensitic 9Cr-1Mo steel compressed by dynamic plastic deformation (DPD) to a strain of 2.3 has been investigated using transmission electron microscopy and electron backscatter diffraction. It is found that the duplex $\langle 111 \rangle + \langle 100 \rangle$ fiber texture formed by DPD is transformed during annealing to a dominant $\langle 111 \rangle$ fiber texture, and that crystallites of the $\langle 111 \rangle$ component have an advantage during both nucleation and growth. Detailed characterization of the microstructural morphology, and estimation of the stored energies in $\langle 111 \rangle$ - and $\langle 100 \rangle$ -oriented regions in deformed and annealed samples, as well as investigations of the growth of recrystallizing grains, are used to analyze the annealing behavior. It is concluded that recrystallization in the given material occurs by a combination of oriented nucleation and oriented growth.

DOI: 10.1007/s11661-016-3626-0

© The Author(s) 2016. This article is published with open access at Springerlink.com

I. INTRODUCTION

Most metals and alloys are subjected to thermomechanical processing, which includes plastic deformation and annealing in various combinations. Annealing after plastic deformation may result in static recrystallization, which is frequently accompanied by changes in the crystallographic texture. For body-centered cubic (bcc) iron-based systems, the deformation texture after compression is dominated by $\langle 100 \rangle$ and $\langle 111 \rangle$ fiber texture components aligned with the compression axis (CA), and it is generally found that the $\langle 100 \rangle$ component weakens during recrystallization, whereas the $\langle 111 \rangle$ fiber texture strengthens significantly.^[1-4]

In a previous study^[3] on a modified ferritic/martensitic 9Cr-1Mo steel where samples were deformed to a strain of 0.5 either by quasistatic compression (QSC) or by dynamic plastic deformation (DPD),^[5,6] it has been found that DPD resulted in a stronger $\langle 111 \rangle + \langle 100 \rangle$ fiber texture and in faster recrystallization than QSC. The faster recrystallization was attributed to a finer boundary spacing and, therefore, a higher energy stored during DPD as compared to QSC.^[3] At a strain of 0.5, the boundary spacings measured by transmission electron microscopy (TEM) in the DPD samples and the QSC samples were in the submicrometer range, 190 nm and 240 nm, respectively.

The aim of the present work is to investigate recrystallization in a sample compressed by DPD to a much higher strain ($\varepsilon = 2.3$) with a finer boundary spacing in the deformed state, and thus with a significantly higher stored energy and driving force for recovery and recrystallization. A preliminary analysis has shown that recrystallization in this material takes place in a highly heterogeneous manner.^[7] It is therefore of interest to link the variations in the deformed microstructure to the recovery and recrystallization taking place in different regions. A spatially resolved analysis of the stored energy distribution after deformation as well as of the changes in this distribution during subsequent annealing is conducted based on EBSD data. In addition, orientation relationships both in the deformed microstructure and between recrystallizing grains and their recovered environment are analyzed in this study. Finally, the EBSD analysis is complemented by a TEM characterization of the sub-grain morphology in the deformed and recovered conditions. This analysis, which takes into account local

ZHENBO ZHANG, formerly Ph.D. Student with the Sino-Danish Center for Education and Research, 8000 Aarhus C, Denmark, is now Postdoctoral Research Associate with the School of Materials, University of Manchester, Manchester M13 9PL, UK. Contact e-mail: zhenbo.zhang@manchester.ac.uk, zbzhang85@gmail.com YUBIN ZHANG, Senior Researcher, is with the Section for Materials Science and Advanced Characterization, Department of Wind Energy, Technical University of Denmark, Risø Campus, 4000 Roskilde, Denmark. OLEG V. MISHIN, Senior Researcher, and DORTE JUUL JENSEN, Professor, are with the Section for Materials Science and Advanced Characterization, Department of Wind Energy, Technical University of Denmark, and also with the Sino-Danish Center for Education and Research. NAIRONG TAO, Professor, is with the Institute of Metal Research, Chinese Academy of Science, Shenyang 110016, China, and also with the Sino-Danish Center for Education and Research. WOLFGANG PANTLEON, Associate Professor, is with the Section for Materials and Surface Engineering, Department of Mechanical Engineering, Technical University of Denmark, 2800 Kgs. Lyngby, Denmark, and also with the Sino-Danish Center for Education and Research.

Manuscript submitted January 19, 2016.

Article published online July 5, 2016

variations in the deformed microstructure, is considered essential for improved understanding and modeling of annealing mechanisms.

II. EXPERIMENTAL

The modified 9Cr-1Mo steel (Table I) sample used in this study was received in the form of a hot extruded rod normalized at 1313 K (1040 °C) for 1.4 hours, tempered at 1043 K (770 °C) for 5 hours and finally stress relieved at 1013 K (740 °C). In the microstructure obtained after this treatment, coarse $M_{23}C_6$ particles were observed at prior austenite grain boundaries and martensite lath boundaries, while small carbonitride particles were distributed randomly in the matrix.^[3,7] The average subgrain size and the average distance between high angle boundaries (HABs) in this as-received condition was 0.7 and 2.4 μm , respectively.^[3,7]

Cylindrical specimens with the CA aligned along the extrusion axis of the as-received rod, and a size of 9 mm in diameter and 12 mm in height were machined for DPD. The specimens were compressed at room temperature to an equivalent (von Mises) strain of 2.3 in five steps at strain rates of 10^2 to 10^3 s^{-1} .

The deformed material was annealed in air at different temperatures between 823 K (550 °C) and 973 K (700 °C) for 1 hour. Another series of samples was obtained by isothermal annealing at 948 K (675 °C) with annealing times in the range between 15 and 90 minutes. In addition, one sample was annealed in vacuum at 923 K (650 °C) for 1 hour, followed by EBSD characterization of randomly chosen regions. This sample was then repeatedly annealed at 923 K (650 °C) for 1 hour in vacuum, and the same regions were inspected again without repolishing.

The deformed and annealed material was investigated in the central part of the samples, in sections perpendicular to the compression plane. Samples were investigated using a JEOL 2000 FX transmission electron microscope operating at 200 kV and a Zeiss Supra 35 field emission gun scanning electron microscope equipped with a Channel 5 EBSD system from HKL Technology. A step size of 20 nm was chosen for studying the deformed microstructure by EBSD. Larger step sizes (50 to 200 nm) were used for texture measurements and for orientation mapping of the annealed samples. The EBSD indexing rate for the sample after DPD was 74 pct. For the annealed samples the indexing rate was at least 85 pct. Because of the limited angular resolution of the EBSD technique,^[8,9] misorientations less than 2 deg were not considered in the orientation maps. Therefore, the boundary spacing measured from the EBSD data was defined as the mean distance

between boundaries with misorientation angles θ greater than 2 deg ($d_{\theta>2\text{deg}}$). Boundaries with misorientations between 2 and 15 deg were classified as low angle boundaries (LABs). Boundaries with misorientations above 15 deg were classified as HABs. Fractions of different texture components were calculated within 10 deg from the exact $\langle 111 \rangle$ and $\langle 100 \rangle$ fibers.

Recrystallized grains were defined using the approach described by Wu and Juul Jensen,^[10] where a grain should satisfy several criteria to be classified as recrystallized: (i) the in-grain pixel-to-pixel misorientation is below 2 deg; (ii) the equivalent circular diameter (ECD) is above 3 μm ; and (iii) the grain is at least partly surrounded by HABs. The volume number density of recrystallized grains was determined as $N_V = N_A/\text{ECD}$ from the area number density N_A of these grains. The EBSD data were also used to determine the boundary area per unit volume, which was applied to estimate the energy stored^[11,12] both in deformed and recovered microstructures. The specific boundary energy of LABs was calculated from the Read–Shockley equation.^[13,14] The specific boundary energy of HABs was assumed to be 617 mJ/m^2 .^[15] Vickers hardness was measured using a load of 1 kg with a 10-second dwell time.

III. RESULTS

A. Deformation Structure After Compression by DPD

A lamellar structure with extended planar boundaries aligned almost perpendicular to the CA and a high dislocation density within elongated subgrains is observed after compression by DPD (see Figure 1). The average spacing between the lamellar boundaries measured using TEM is 98 nm.

Analysis of selected area diffraction patterns and the EBSD data indicate that lamellae of the $\langle 111 \rangle$ or $\langle 100 \rangle$ fiber texture components are arranged in alternating bands (see Figures 1 and 2(a)) with an average width of 0.3 μm . The boundary spacing $d_{\theta>2\text{deg}}$ measured along the CA within the $\langle 111 \rangle$ bands is slightly finer than that within the $\langle 100 \rangle$ bands, 110 and 116 nm, respectively. It should be noted that these values do not take into account boundaries between the $\langle 111 \rangle$ and $\langle 100 \rangle$ bands. The average $d_{\theta>2\text{deg}}$ along the CA calculated taking into account all boundaries identified in the orientation maps is 110 nm. The average spacing between HABs determined from the EBSD data is 200 nm. No appreciable difference in the frequency and the spatial distribution of particles is found in the regions of $\langle 111 \rangle$ or $\langle 100 \rangle$ texture components. The two texture components form a duplex $\langle 111 \rangle + \langle 100 \rangle$ fiber texture, where the $\langle 100 \rangle$ component is somewhat stronger than the $\langle 111 \rangle$ component (see Figure 2(b)).

Table I. Chemical Composition (Weight Percent) of the Modified 9Cr-1Mo Steel as Determined by Glow Discharge Optical Emission Spectroscopy

| C | Cr | Mo | V | Ni | Nb | W | Si | Mn | P | S | Fe |
|------|------|------|------|------|------|------|------|------|------|-------|---------|
| 0.11 | 8.20 | 0.98 | 0.20 | 0.16 | 0.07 | 0.01 | 0.31 | 0.51 | 0.02 | <0.01 | balance |

B. Evolution During Isochronal Annealing

The microstructural evolution during annealing at different temperatures for 1 hour is shown in Figures 3 and 4. It is seen that at temperatures below 923 K (650 °C), the microstructure evolves primarily by subgrain coarsening, though a number of small (between 1 and 3 μm) strain-free recrystallization nuclei are present after annealing at 873 K (600 °C) and 898 K (625 °C) with a total area fraction of 1 and 4 pct, respectively. Whereas most subgrains become less elongated during the coarsening, regions with highly elongated subgrains, similar to those in the as-deformed material, are still observed in the recovered microstructure (Figures 4(a) and (b)). TEM diffraction analysis shows that the regions with highly elongated subgrains belong to the $\langle 100 \rangle$ component (see Figure 4(a)).

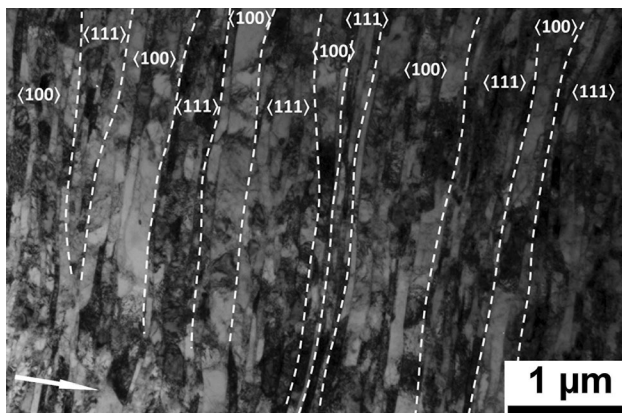


Fig. 1—TEM image from the cross section of the deformed sample. Dashed lines mark alternating bands in the lamellar structure belonging to either the $\langle 100 \rangle$ fiber texture component or the $\langle 111 \rangle$ fiber texture component. The CA is indicated by an arrow.

The coarsening results in significant softening of the material (Figure 5(a)). As expected, the boundary spacing increases with increasing annealing temperature. The average boundary spacing measured in the recovered regions within the $\langle 111 \rangle$ bands remains slightly less than that within the $\langle 100 \rangle$ bands only at temperatures up to 873 K (600 °C) (see Figure 5(b)). After annealing at 923 K (625 °C) and 923 K (650 °C) there is almost no difference in the boundary spacing within the recovered regions of the two texture components. After annealing at 948 K (675 °C), the spacing within recovered $\langle 111 \rangle$ bands exceeds that within $\langle 100 \rangle$ bands (Figure 5(b)).

No significant change in texture is observed for temperatures below 923 K (650 °C) (Figure 6). Annealing at 923 K (650 °C) for 1 hour results in pronounced recrystallization (see Figures 3(c) and 4(c) and (d)) with an area fraction of recrystallized material $f_{\text{Rex}} = 12$ pct. Most of the recrystallizing grains in Figure 3(c) belong to the $\langle 111 \rangle$ component, and the intensity of the $\langle 111 \rangle$ component increases at the expense of the $\langle 100 \rangle$ component (see Figure 6(c)). For the higher temperature of 948 K (675 °C), f_{Rex} increases to 78 pct. After annealing at 973 K (700 °C) for 1 hour the material is almost fully recrystallized ($f_{\text{Rex}} = 99$ pct, see Figure 3(d)). The texture of this almost fully recrystallized sample is dominated by the $\langle 111 \rangle$ component (see Figure 6(d)), whereas the $\langle 100 \rangle$ component is very weak.

C. Evolution During Isothermal Annealing

For a statistical characterization of both recovery and recrystallization during isothermal annealing, a temperature of 948 K (675 °C) and annealing durations in the range from 15 to 90 minutes were chosen. In addition to this statistical analysis, several regions containing 16 recrystallizing grains were investigated using the EBSD technique after 1 hour at 923 K (650 °C), where the

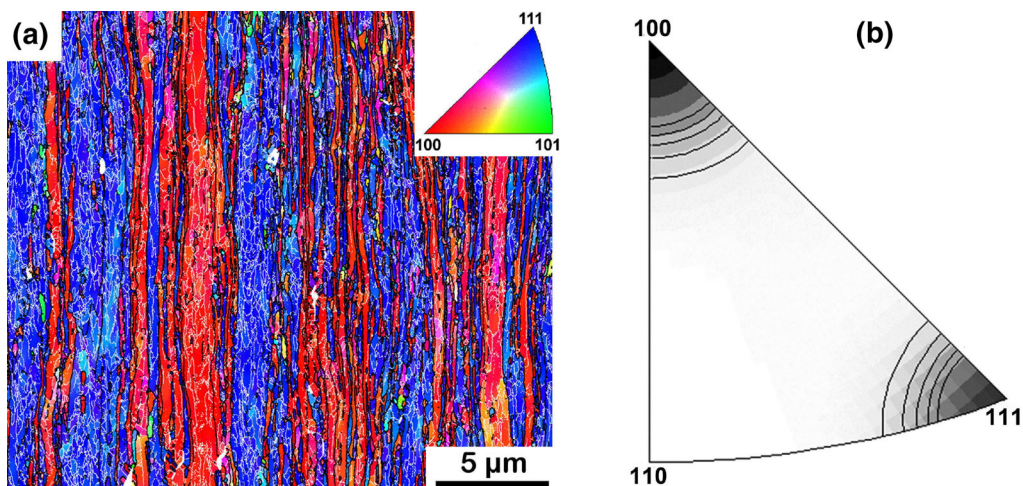


Fig. 2—Microstructure and texture of the deformed sample determined by EBSD: (a) orientation map, where different colors correspond to different crystallographic directions along the CA as shown in the inverse pole figure (IPF) (see the inset). The dominant $\langle 100 \rangle$ and $\langle 111 \rangle$ fiber texture components are shown in red and blue, respectively. LABs and HABs are shown as white and black lines, respectively. In the orientation map, the CA is parallel to the scale bar; (b) IPF showing crystallographic directions along the CA from an area of $\sim 1.2 \text{ mm}^2$. The maximum intensity of the $\langle 100 \rangle$ and $\langle 111 \rangle$ components is 15 and 10 times random, respectively. Contour lines are 1, 2, 3, 4, and 5 times random (Color figure online).

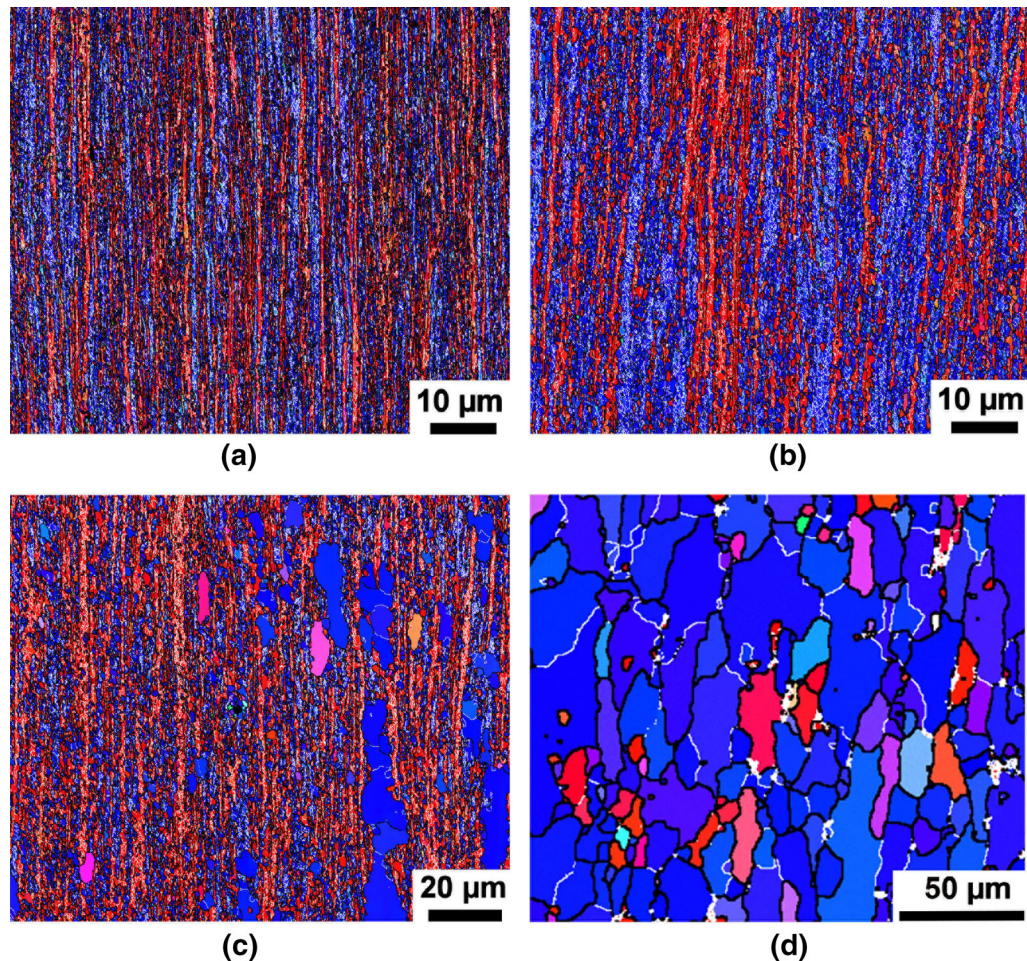


Fig. 3—Orientation maps obtained by EBSD from the sample annealed at different temperatures for 1 h: (a) 823 K (550 °C), (b) 873 K (600 °C), (c) 923 K (650 °C), and (d) 973 K (700 °C). Different colors in the maps correspond to different crystallographic directions along the CA as shown in the inset in Figure 2(a). LABs and HABs are shown as white and black lines, respectively. The CA is parallel to the scale bar (Color figure online).

same regions were reexamined after additional annealing at 923 K (650 °C) for 1 hour without repolishing to identify migrating boundaries at the early stage of recrystallization.

1. Statistical characterization of changes during annealing at 948 K (675 °C)

Orientation maps from different regions of the material annealed at 948 K (675 °C) are shown in Figure 7. It is apparent that a number of small (between 3 and 10 μm) recrystallizing grains are present in the microstructure already after 15 minutes of annealing at 948 K (675 °C) (Figure 7(a)). The area fraction of the recrystallizing grains in this condition is 4 pct, and most of these grains have orientations of the $\langle 111 \rangle$ component. The hardness is reduced from 365 HV1 in the DPD sample to 243 HV1 after 15 minutes of annealing (Figure 8). Further annealing increases the number, average size and the area fraction of recrystallizing grains, and leads to a further softening of the material (see Figures 7, 8 and 9).

Recrystallization occurs heterogeneously, with recrystallizing grain clustering in the form of bands

perpendicular to the CA (Figure 7(b)). Figure 9(a) indicates that for all annealing durations the number density of the $\langle 111 \rangle$ recrystallizing grains is much greater than the corresponding number density of the $\langle 100 \rangle$ grains. Additionally, the average size of the $\langle 111 \rangle$ recrystallizing grains is significantly larger than that of the $\langle 100 \rangle$ grains (see Figure 9(b)). For instance, the average recrystallized grain sizes after annealing for 30 minutes (total $f_{\text{Rex}} = 26$ pct) are 6.5 and 3.7 μm for the $\langle 111 \rangle$ grains and the $\langle 100 \rangle$ grains, respectively. After 90 minutes at 948 K (675 °C) (total $f_{\text{Rex}} = 81$ pct), the average recrystallized grain sizes increase to 9.0 and 5.7 μm for the $\langle 111 \rangle$ and $\langle 100 \rangle$ components, respectively. The larger average size and higher frequency of the recrystallizing $\langle 111 \rangle$ grains result in a larger area fraction of such grains (see Figure 9(c)).

2. Monitoring of changes during annealing at 923 K (650 °C) in the same-region experiment

Examples of the orientation maps representing the partially recrystallized microstructure obtained after annealing at 923 K (650 °C) for 1 hour and examined again after an additional hour of annealing at the same

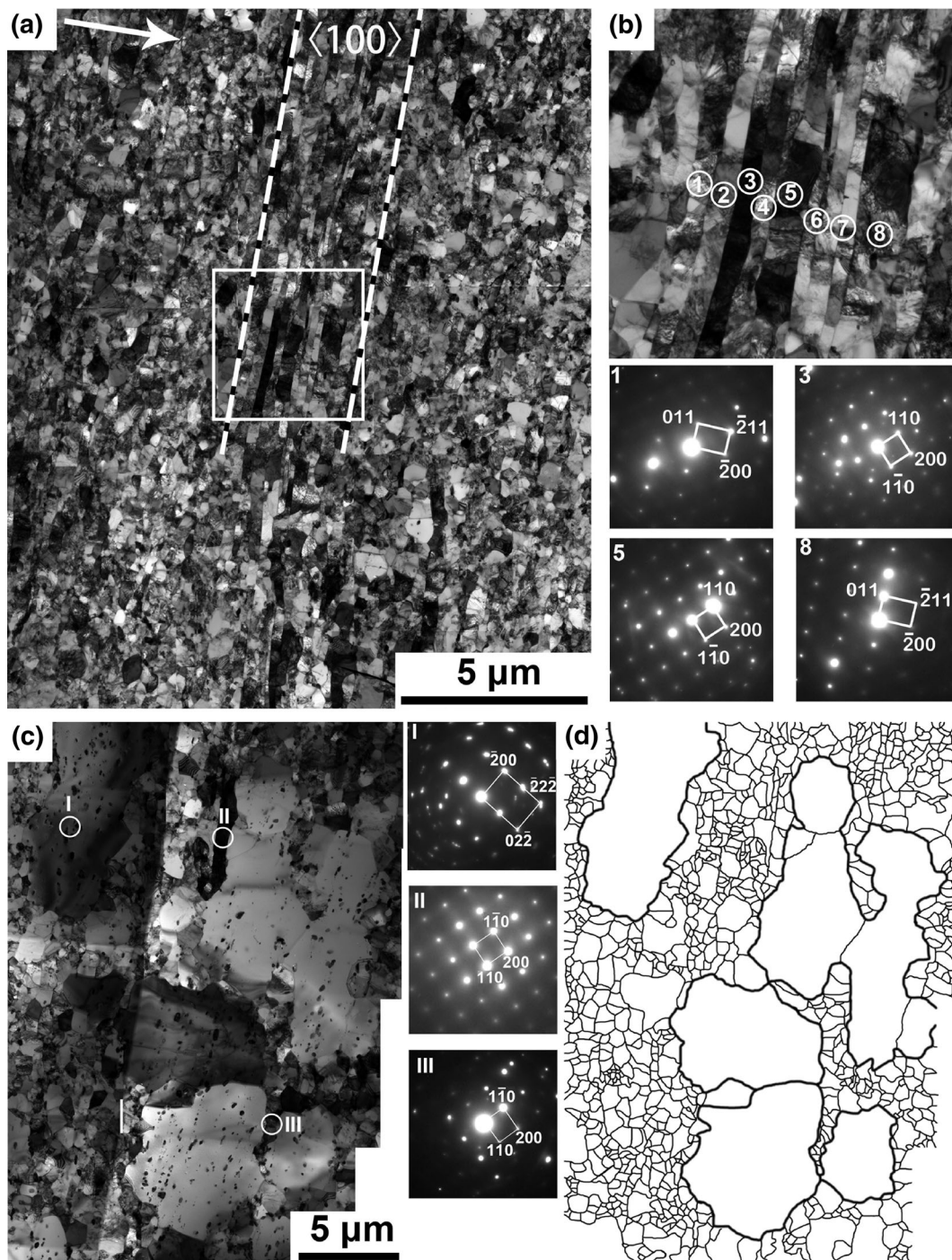


Fig. 4—Microstructures observed using TEM in the sample after annealing for 1 h at 873 K (600 °C) (a, b) and 923 K (650 °C) (c, d). A $\langle 100 \rangle$ -oriented band containing highly elongated subgrains is indicated by dashed lines in (a), and a small region of this band marked by a frame is enlarged in (b), where selected area diffraction (SAD) patterns for individual lamellae 1, 3, 5, and 8 are also shown. (d) is a schematic illustration of the microstructure shown in (c). Large recrystallized grains in (c, d) belong to the $\langle 111 \rangle$ fiber texture component, whereas the crystallographic orientation of the neighboring matrix in (c, d) belongs to the $\langle 100 \rangle$ component as follows from SAD patterns for regions I, II, and III. The CA is indicated by an arrow.

temperature are given in Figure 10. In this figure, “I” and “II” refer to identical areas analyzed after 1 and 2 hours of annealing at 923 K (650 °C). Numbers 1 to 6 mark six $\langle 111 \rangle$ grains growing predominantly into the recovered $\langle 111 \rangle$ matrix. Therefore, boundaries between these grains and the $\langle 111 \rangle$ matrix are referred here to as

$\langle 111 \rangle / \langle 111 \rangle$ boundaries. It is evident from Figure 10 that migrating $\langle 111 \rangle / \langle 111 \rangle$ boundaries are mostly HABs. Although boundaries between $\langle 111 \rangle$ grains and $\langle 100 \rangle$ matrix ($\langle 111 \rangle / \langle 100 \rangle$ boundaries) are also HABs, these boundaries mostly do not migrate during the additional annealing treatment.

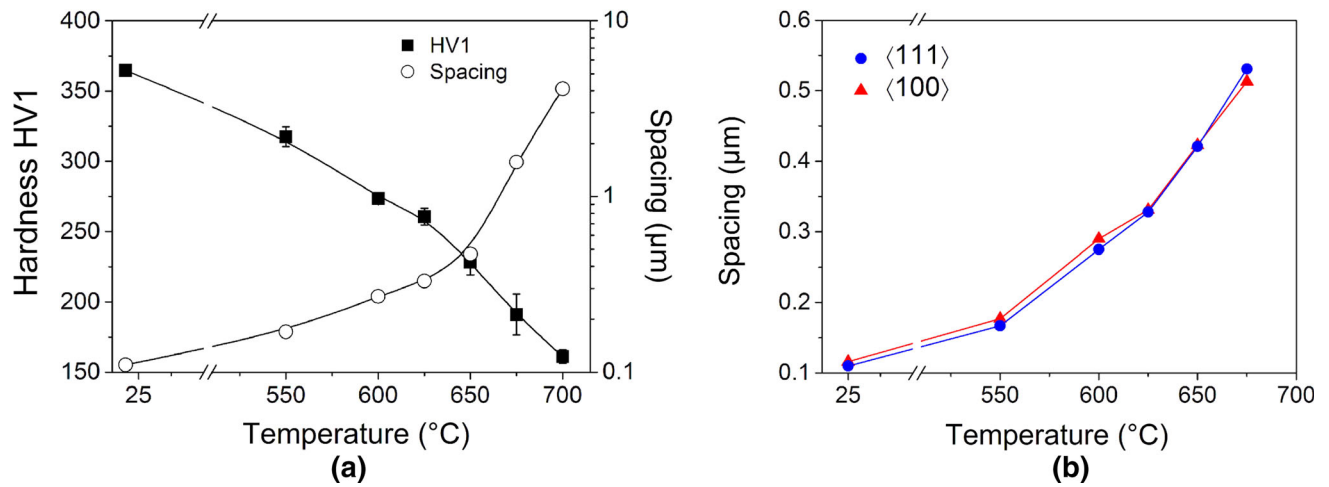


Fig. 5—Effect of annealing at different temperatures for 1 h on the Vickers hardness and the average boundary spacing along the CA in the orientation maps obtained by EBSD (a), and the spacing along the CA measured separately within recovered $\langle 100 \rangle$ and $\langle 111 \rangle$ regions (b). The error bars in (a) correspond to the standard deviation of the sampling distribution.

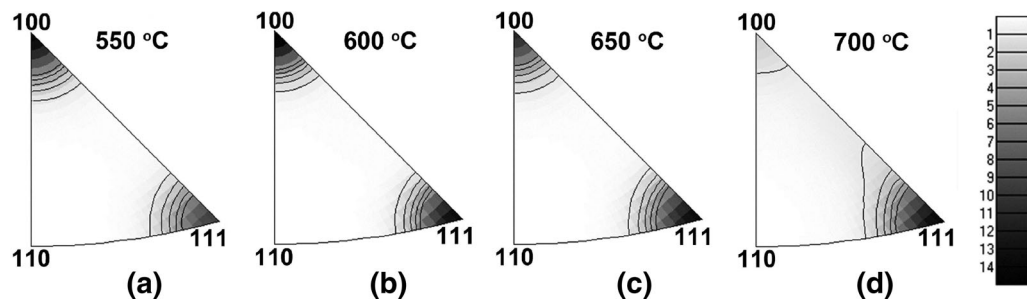


Fig. 6—Texture evolution during annealing at different temperatures for 1 h: (a) 823 K (550 °C), (b) 873 K (600 °C), (c) 923 K (650 °C), and (d) 973 K (700 °C) illustrated by inverse pole figures for the crystallographic direction along the CA. Contour lines are 1, 2, 3, 4, and 5 times random.

Misorientation distributions for all boundaries between the 16 recrystallizing $\langle 111 \rangle$ grains, identified in this same-region experiment, and the recovered matrix of the $\langle 111 \rangle$ or $\langle 100 \rangle$ components are presented in Figures 11(a) and (b). It is seen that there is a significant difference between the misorientations of $\langle 111 \rangle / \langle 111 \rangle$ and $\langle 111 \rangle / \langle 100 \rangle$ boundaries: for the former the dominant misorientation axis is $\langle 111 \rangle$, while for the latter the highest concentration of misorientation axes is near $\langle 110 \rangle$. In addition, the angular distribution of the $\langle 111 \rangle / \langle 111 \rangle$ boundaries is much broader than that of the $\langle 111 \rangle / \langle 100 \rangle$ boundaries. These differences are consistent with theoretical distributions describing misorientations between $\langle 111 \rangle$ -oriented grains and the $\langle 111 \rangle$ or $\langle 100 \rangle$ fiber texture components.

Figure 11(c) shows the distribution of misorientations only across boundaries that actually have migrated during the additional annealing treatment. This distribution includes all misorientations between a growing grain and each pixel in the recovered matrix consumed during the additional annealing step (see Reference 16 for more details of the calculation approach). The distribution is rather broad, where the majority of boundary misorientations can be described as 20 to 60 deg $\langle 111 \rangle$.

The fraction of 20 to 30 deg $\langle 111 \rangle$ boundaries, which have been previously found to form preferentially between the matrix and recrystallizing grains in some rolled bcc single crystals,^[17,18] is 22 pct (calculated allowing a deviation of 10 deg from the exact 25 deg $\langle 111 \rangle$ misorientation). The fraction of 27 deg $\langle 110 \rangle$ boundaries, typically considered to be high mobility boundaries in bcc steels,^[19,20] is only 4.6 pct.

IV. DISCUSSION

A. Structural Refinement During DPD

DPD has previously been shown to result in more pronounced structural refinement than deformation at low strain rates, which has been attributed to a higher density of dislocations forming more finely spaced dislocation boundaries than in materials after QSC.^[3,21,22] Although the microstructure of the QSC sample deformed to a strain of 2.3 has not been characterized in the present work, the hardness data available after this strain indicate that the QSC sample is considerably softer (348 HV1) than the DPD sample (365 HV1), which is consistent with earlier observations for the samples deformed to a lower strain^[3] and which suggests that

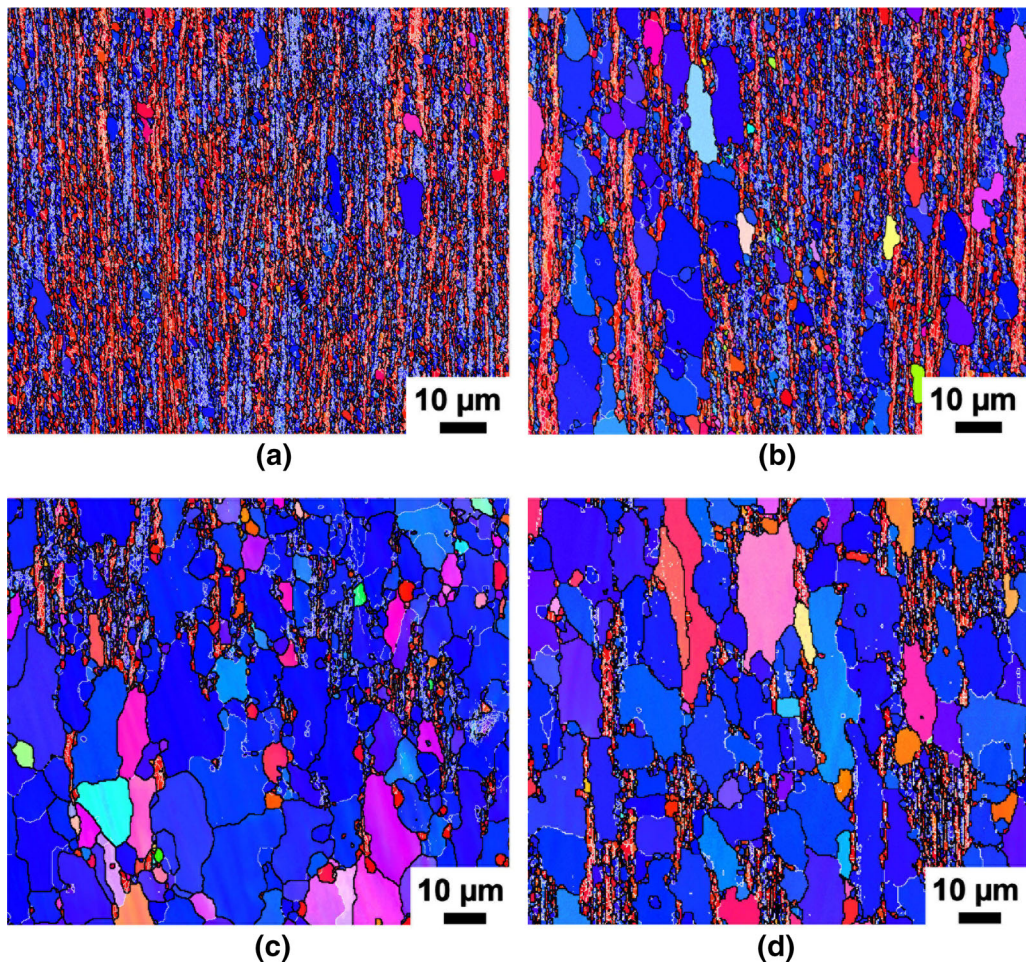


Fig. 7—Orientation maps obtained by EBSD for the sample annealed at 948 K (675 °C) for (a) 15 min, (b) 30 min, (c) 60 min, and (d) 90 min. Different colors in the maps correspond to different crystallographic directions along the CA as shown in the inset in Fig. 2(a). LABs and HABs are shown as white and black lines, respectively. The CA is parallel to the scale bar (Color figure online).

the structural refinement by DPD is more effective than that by QSC also at a strain of 2.3.

Compared to a previous study of the present material DPD-processed to a strain of 0.5,^[3,7] where a dislocation cell structure was observed to have an average boundary spacing of 0.2 μm, the sample studied in the present work contains a much more refined lamellar structure with a boundary spacing of only 0.1 μm. It is therefore apparent that during DPD the initial tempered martensite structure evolves first to a typical cell structure at low strains and then to a nanoscale lamellar structure as the strain increases. The lamellar structure observed at a strain of 2.3 is arranged in alternating $\langle 111 \rangle$ and $\langle 100 \rangle$ bands with an average width of 0.3 μm. The HAB spacing is smaller—approximately 0.2 μm, which is similar to the expected grain thickness (0.24 μm) after a strain 2.3 (note that the HAB spacing prior to DPD was 2.4 μm^[3]).

Considering the differences between the regions of the different texture components, it is found that the $\langle 111 \rangle$ regions are characterized by a smaller boundary spacing and, therefore, have a higher stored energy than the $\langle 100 \rangle$ regions. Calculations based on the EBSD data show that the energy stored in the form of boundaries is

indeed greater in the $\langle 111 \rangle$ regions than in the $\langle 100 \rangle$ regions, 6.0 and 4.2 MJ/m³, respectively. This considerable difference in the stored energy for the bands of the different texture components is attributed to the difference in their Taylor factors, where $M_{\langle 111 \rangle} > M_{\langle 100 \rangle}$,^[23] leading to an increased slip activity in the $\langle 111 \rangle$ regions and hence a larger density of dislocations forming deformation-induced boundaries.

B. Recovery

Recovery in the modified 9Cr-1Mo steel is accompanied by coarsening of the deformed microstructure driven by the reduction in the boundary energy. Calculations based on the EBSD data show that the stored energy is significantly reduced during coarsening (see Figure 12), and that the reduction rate is higher in the $\langle 111 \rangle$ regions, for which the initial stored energy was greater than that for the $\langle 100 \rangle$ regions. This observation is in agreement with our recent results obtained on PM2000 annealed after DPD^[4] and with findings obtained on commercial purity aluminum annealed after heavy rolling,^[24] where more pronounced recovery was observed in high-energy texture bands compared to

low-energy texture bands. Considering the contributions of HABs and LABs separately (see insets in Figure 12), it is clear that the different reduction in the stored energy for the different regions is predominantly caused by differences in the loss of LABs.

The lower driving force for coarsening in the $\langle 100 \rangle$ bands in the DPD-processed steel may explain the

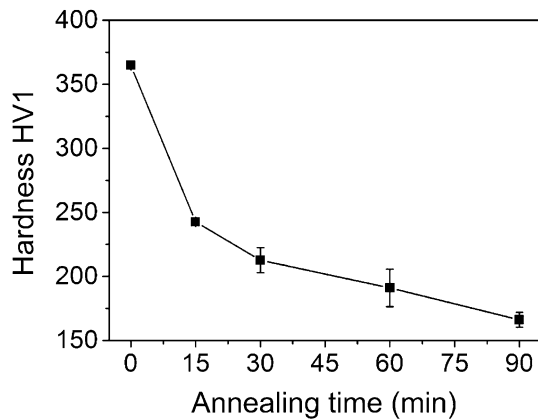


Fig. 8—Evolution of Vickers hardness during annealing at 948 K (675 °C). The error bars correspond to the standard deviation of the sampling distribution.

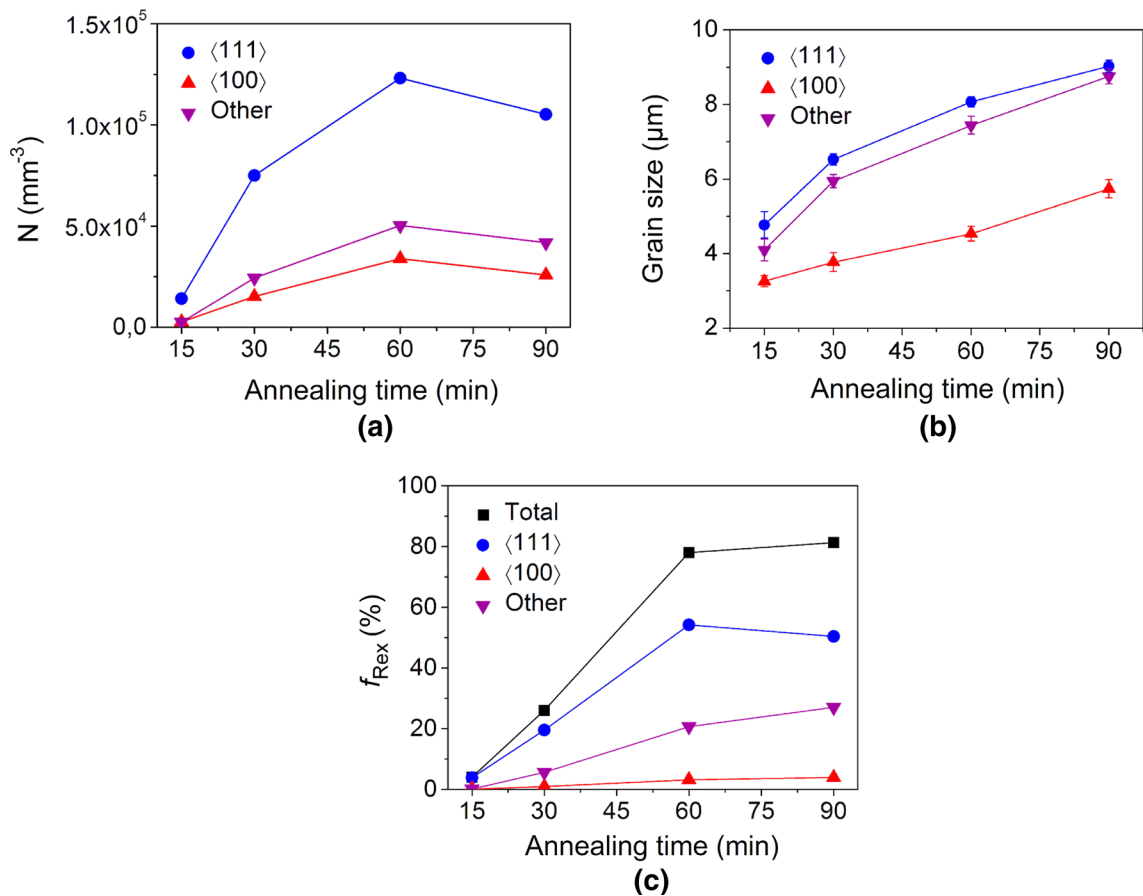


Fig. 9—Parameters of recrystallized grains with different crystallographic orientations in the sample annealed at 948 K (675 °C) for different periods of time: (a) number density; (b) average grain size expressed as ECD; (c) area fraction. The error bars in (b) correspond to the standard deviation of the mean.

presence of the retained lamellar structure within the $\langle 100 \rangle$ regions after annealing at 873 K (600 °C) for 1 hour (Figure 4(a) and (b)), whereas no such structures are seen within the $\langle 111 \rangle$ regions. A result of the more pronounced recovery within the $\langle 111 \rangle$ regions is that the difference between the stored boundary energy in the $\langle 111 \rangle$ and $\langle 100 \rangle$ regions is reduced significantly prior to recrystallization.

Microstructural analysis indicates that pronounced recrystallization takes place when the stored boundary energy within both $\langle 111 \rangle$ and $\langle 100 \rangle$ regions is rather similar (see Figure 12). It should however be noted that the very first recrystallization nuclei appear when the difference in the stored energy between these regions is still appreciable. For example, in the microstructure after 1 hour at 873 K (600 °C), where the nuclei occupy 1 pct of the area, the stored energy within the $\langle 111 \rangle$ and $\langle 100 \rangle$ bands is 2.7 and 2.0 MJ/m³, respectively.

C. Recrystallization

During recrystallization $\langle 111 \rangle$ nuclei develop within the $\langle 111 \rangle$ texture bands, while $\langle 100 \rangle$ nuclei are observed within the $\langle 100 \rangle$ bands, as seen, for instance, in Figure 7(a). These observations are consistent with the standard concept of nucleation, *i.e.*, nucleation is closely

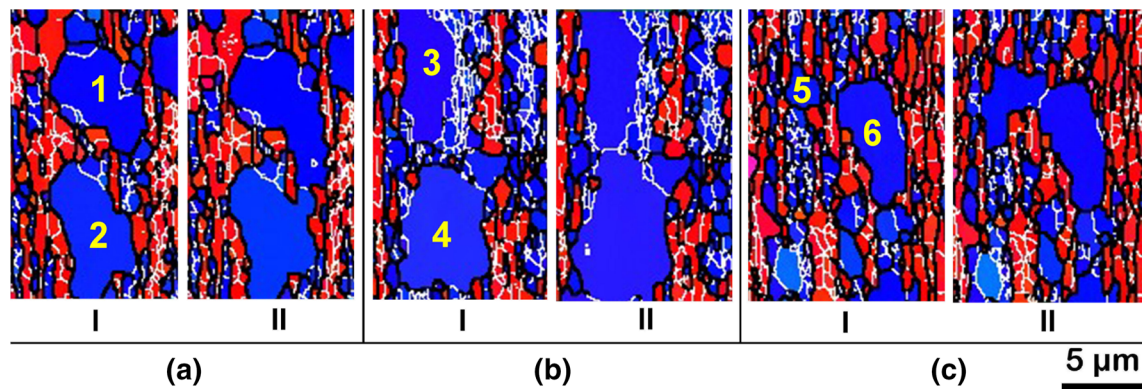


Fig. 10—Three regions, (a), (b) and (c), investigated using the EBSD technique first after annealing at 923 K (650 °C) for 1 h (marked “I”) and again after an additional hour (marked “II,” total annealing time 2 h). Six recrystallizing grains (out of the 16 grains analyzed in the same-region experiment) are numbered 1 to 6 in the maps marked “I.” Different colors in the maps correspond to different crystallographic directions along the CA as shown in the inset in Fig. 2(a). LABs and HABs are shown as white and black lines, respectively. The CA is parallel to the scale bar (Color figure online).

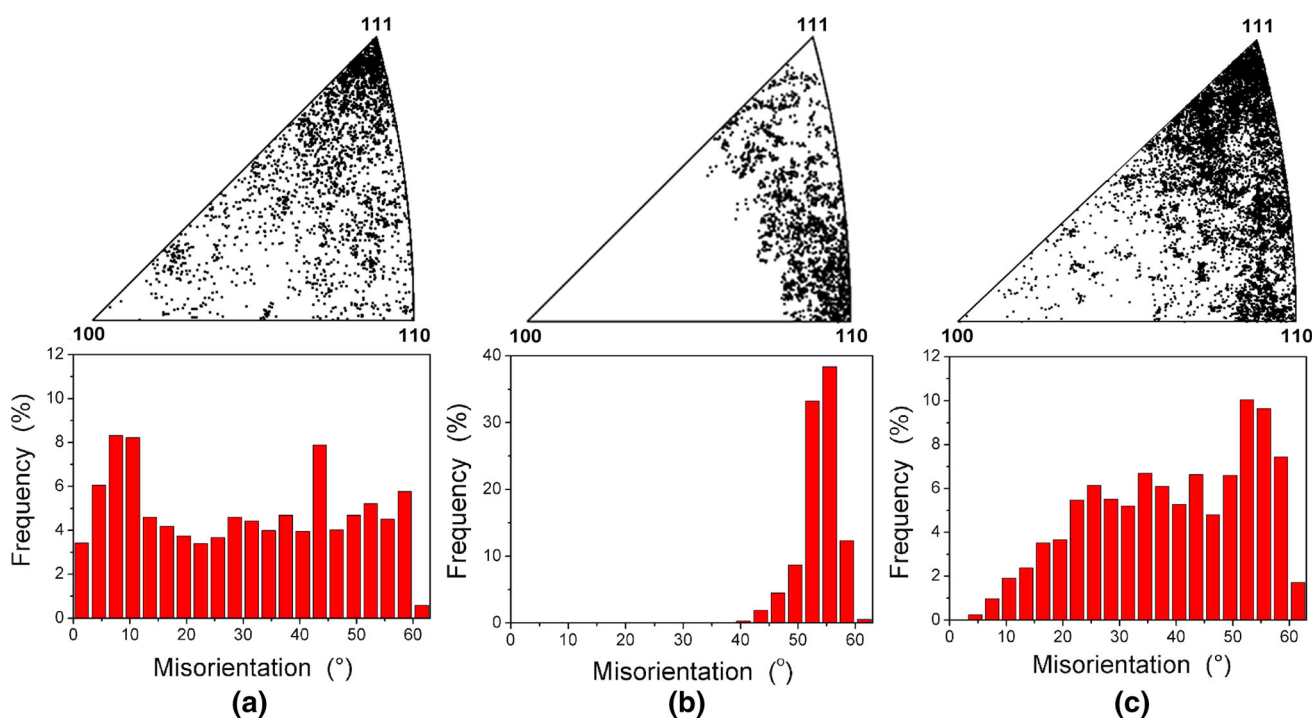


Fig. 11—Distributions of misorientation angles and axes for boundaries in the same-region experiment: misorientations across all boundaries between the 16 recrystallizing grains of the $\langle 111 \rangle$ texture and the matrix of either the $\langle 111 \rangle$ component (a) or the $\langle 100 \rangle$ component (b); (c) misorientations only across the migrating boundaries.

related to the microstructure in which it occurs by growth from preexisting subgrains.^[15] Nevertheless, the number of the $\langle 111 \rangle$ -oriented nuclei is found to be significantly greater than the number of the $\langle 100 \rangle$ -oriented nuclei. Altogether, after annealing at 948 K (675 °C) for 1 hour, 59 and 15 pct of all nuclei belong to the $\langle 111 \rangle$ and $\langle 100 \rangle$ fiber texture components, respectively. These relative frequencies are larger than the orientation probabilities for the texture components expected for a *bcc* material with a random texture. The increased relative frequencies of the $\langle 111 \rangle$ and $\langle 100 \rangle$ nuclei result from the strong duplex texture, with the $\langle 111 \rangle$ and $\langle 100 \rangle$ components representing 37 and 49 pct

of all orientations, respectively. If nucleation of the $\langle 111 \rangle$ - and $\langle 100 \rangle$ -oriented grains were simply related to these area fractions in the deformation texture (which does not significantly change during recovery), the relative frequencies of the $\langle 111 \rangle$ and $\langle 100 \rangle$ nuclei would have been similar to the fractions of the $\langle 111 \rangle$ and $\langle 100 \rangle$ components in the deformation texture. The observation that the relative frequency of the $\langle 111 \rangle$ -oriented nuclei is much higher than the area fraction of the $\langle 111 \rangle$ deformation matrix implies that nucleation of the $\langle 111 \rangle$ grains is preferential. Combined with the fact that the frequency of $\langle 100 \rangle$ -oriented nuclei is less than the area fraction of the $\langle 100 \rangle$ matrix, this suggests that

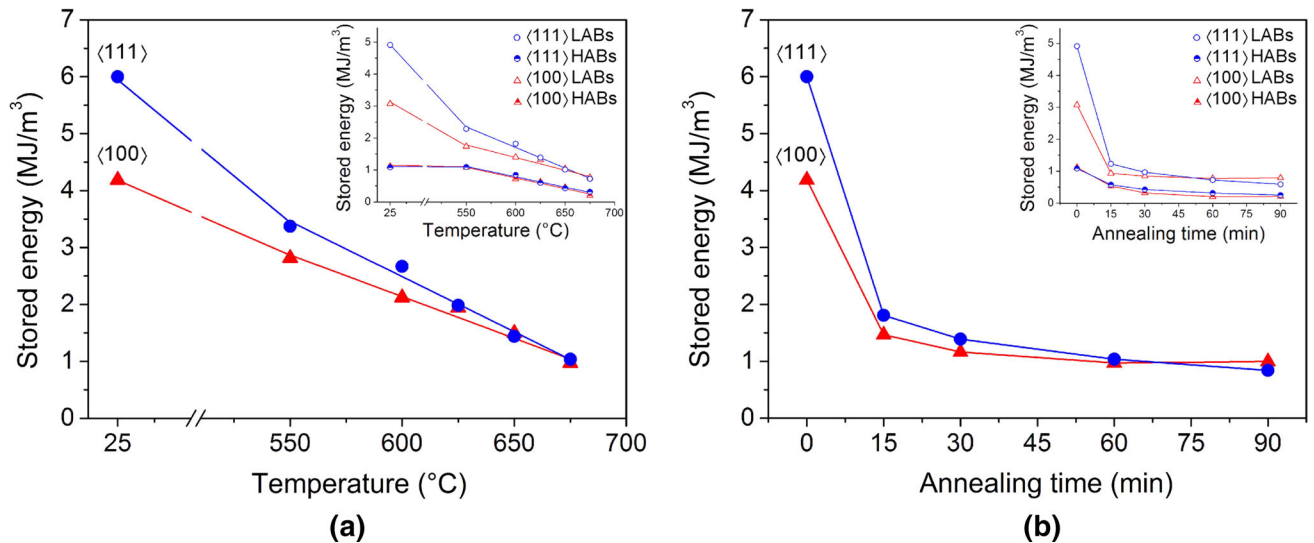


Fig. 12—Evolution of the stored boundary energy calculated from the EBSD data separately for recovered $\langle 100 \rangle$ and $\langle 111 \rangle$ regions: (a) during annealing at different temperatures for 1 h; (b) during isothermal annealing at 948 K (675 °C). Contributions of HABs and LABs are shown in the insets.

nucleation in the DPD-processed steel is orientation dependent.

Oriented nucleation has previously been described as the key process determining recrystallization textures in iron and bcc steels deformed by rolling.^[2,25–29] According to Every and Hatherly,^[29] who studied texture evolution during recrystallization in a warm-rolled low-carbon steel, preferential nucleation of $\langle 111 \rangle$ //ND-oriented grains is due to a higher stored energy in the deformed microstructure of this crystallographic orientation. Significant effects of the difference in the stored energy between regions having different orientations on recovery and recrystallization in rolled steels have also been reported by other researchers.^[30–35] Our analysis of the orientation-dependent distribution of the stored energy in the DPD-processed material is generally consistent with those obtained on the rolled bcc materials: after deformation the stored energy calculated for the $\langle 111 \rangle$ -oriented regions is much higher than that for the $\langle 100 \rangle$ -oriented regions (Figure 12). However, as mentioned in Subsection IV-B, the difference in the stored energy between the $\langle 111 \rangle$ and $\langle 100 \rangle$ regions is significantly reduced during recovery. It is therefore apparent that the preferential nucleation of the $\langle 111 \rangle$ grains may not be rationalized solely based on the large difference in the stored energy in the as-deformed state. It is proposed that the difference in morphological characteristics of recovered subgrains of different texture components (see Figure 4(a)) may also play a role, and that nuclei develop more easily within the almost equiaxed recovered structures of the $\langle 111 \rangle$ component than within the lamellar structures of the $\langle 100 \rangle$ component having a similar stored energy.

To analyze whether the growth of recrystallized grains in the present material is also sensitive to the crystallographic orientation, growth rates for a series of specimens partially recrystallized at 948 K (675 °C) were analyzed using the extended Cahn–Hagel approach,^[36]

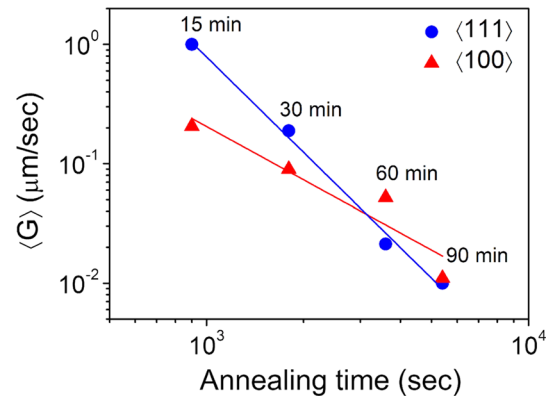


Fig. 13—Growth rates of $\langle 100 \rangle$ - and $\langle 111 \rangle$ -oriented recrystallized grains calculated using the extended Cahn–Hagel method based on the EBSD data for the samples annealed at 948 K (675 °C) for different times.

which enabled the calculation of impingement-corrected average growth rates for grains of different orientations. The growth rates obtained using this approach reveal that during the early stage of recrystallization the $\langle 111 \rangle$ grains grow significantly (up to 5 times) faster than the $\langle 100 \rangle$ grains (see Figure 13) and that the difference in the growth rates between the $\langle 111 \rangle$ and $\langle 100 \rangle$ grains diminishes with increasing annealing time.

The different growth rates cannot be attributed to the effects of particles as their frequency appeared similar in the $\langle 111 \rangle$ and $\langle 100 \rangle$ regions. Therefore, boundary pinning by particles^[7] in these regions is expected to be similar. The oriented growth of the $\langle 111 \rangle$ grains can also not be attributed to a few specific misorientations, such as ~ 27 deg $\langle 110 \rangle$ or 20 to 30 deg $\langle 111 \rangle$, generally considered favorable for growth of recrystallizing grains in bcc metals and steels. In contrast, the migrating boundaries in the annealed DPD sample are characterized by a large variety of misorientations (see

Figure 11(c)), which is consistent with the data obtained by Hutchinson and Ryde^[26] for rolled *bcc* steels. It is suggested that the different morphology of the recovered $\langle 111 \rangle$ and $\langle 100 \rangle$ subgrains may affect the growth rate of recrystallizing grains. If a recrystallization boundary migrates into a deformation structure with equiaxed subgrains, an almost constant driving force in all directions is expected. However, if such a boundary migrates into a lamellar structure, the driving force is anisotropic. In this case, the migration rate is different in different directions and particularly low for segments of the recrystallization boundary, which are parallel to the lamellar boundaries, but at some distance from them. This may explain why $\langle 111 \rangle$ grains grow more rapidly into the equiaxed $\langle 111 \rangle$ regions than $\langle 100 \rangle$ grains growing into the lamellar $\langle 100 \rangle$ regions in the beginning of recrystallization. Apparently, the significantly faster initial growth of the $\langle 111 \rangle$ grains, fully or partially surrounded by HABs (see Figure 11(c)), results in a larger final size of these grains and promotes the very strong $\langle 111 \rangle$ recrystallization texture.

V. CONCLUSIONS

Changes in the microstructure and texture during annealing of a modified 9Cr-1Mo steel compressed *via* dynamic plastic deformation (DPD) at a high strain rate have been studied using both TEM and EBSD techniques with special attention to *local* microscale processes. The following conclusions are obtained from this study.

1. DPD to a strain of 2.3 results in a duplex $\langle 111 \rangle + \langle 100 \rangle$ fiber texture and a lamellar structure with an average spacing of about 100 nm between lamellar boundaries. Estimation of the stored energy based on the EBSD data show that in the as-deformed condition, the stored energy within $\langle 111 \rangle$ regions is significantly higher than that within $\langle 100 \rangle$ regions.
2. During annealing the microstructure first recovers and coarsens, which causes softening and reduction in the stored energy. This reduction is found to be faster within the $\langle 111 \rangle$ regions than within the $\langle 100 \rangle$ regions. As a result, the stored energy within the recovered structures of the two texture components becomes quite similar prior to the onset of pronounced recrystallization. In the recovered microstructure, $\langle 111 \rangle$ -oriented subgrains are almost equiaxed, whereas highly elongated subgrains can still be found in the $\langle 100 \rangle$ regions.
3. Examination of samples annealed at different temperatures for 1 hour reveals that small recrystallization nuclei appear at 873 K (600 °C), whereas recrystallized grains greater than 3 μm are observed at temperatures of 923 K (650 °C) and above. At 948 K (675 °C) the microstructure is partially recrystallized already after 15 minutes annealing. Recrystallizing grains of the $\langle 111 \rangle$ component have an advantage during both nucleation and growth. Consequently, both oriented nucleation and oriented growth contribute to the strong $\langle 111 \rangle$ recrystallization texture development.

4. Considering that the difference in the stored energy between the recovered $\langle 111 \rangle$ and $\langle 100 \rangle$ regions is small at the onset of pronounced recrystallization, it is suggested that the preferential nucleation of the $\langle 111 \rangle$ grains is not only because of the higher energy stored in the $\langle 111 \rangle$ bands, but may also be favored by the almost equiaxed shape of recovered $\langle 111 \rangle$ subgrains as compared to recovered $\langle 100 \rangle$ regions which retained the lamellar structure with extended planar boundaries. It is suggested that the different morphology of the recovered $\langle 111 \rangle$ and $\langle 100 \rangle$ microstructures may also affect the growth rates leading to preferred growth of the $\langle 111 \rangle$ grains.
5. Analysis of migrating boundaries of the rapidly growing $\langle 111 \rangle$ grains indicates that the distribution of misorientation angles for these boundaries is broad and thus not limited to any special misorientation generally considered favorable for growth of recrystallizing grains.

ACKNOWLEDGMENTS

The authors acknowledge the support from the Sino-Danish Center for Education and Research. The authors also gratefully acknowledge the support from the Danish National Research Foundation (Grant No. DNRF86-5) and the National Natural Science Foundation of China (Grant No. 51261130091) to the Danish-Chinese Center for Nanometals. The authors would like to thank Professor A. Godfrey and Dr. F.X. Lin for helpful discussions.

OPEN ACCESS

This article is distributed under the terms of the Creative Commons Attribution 4.0 International License (<http://creativecommons.org/licenses/by/4.0/>), which permits unrestricted use, distribution, and reproduction in any medium, provided you give appropriate credit to the original author(s) and the source, provide a link to the Creative Commons license, and indicate if changes were made.

REFERENCES

1. H. Hu: *Texture*, 1974, vol. 1, pp. 233–58.
2. I.L. Dillamore, H. Kato, and K. Haslam: *Texture*, 1974, vol. 1, pp. 151–56.
3. Z.B. Zhang, O.V. Mishin, N.R. Tao, and W. Pantleon: *Mater. Sci. Technol.*, 2015, vol. 31, pp. 715–21.
4. Z.B. Zhang, N.R. Tao, O.V. Mishin, and W. Pantleon: *J. Mater. Sci.*, 2016, vol. 51, pp. 5545–55.
5. Y.S. Li, N.R. Tao, and K. Lu: *Acta Mater.*, 2008, vol. 56, pp. 230–41.
6. F.K. Yan, G.Z. Liu, N.R. Tao, and K. Lu: *Acta Mater.*, 2012, vol. 60, pp. 1059–71.
7. Z.B. Zhang, O.V. Mishin, N.R. Tao, and W. Pantleon: *J. Nucl. Mater.*, 2015, vol. 458, pp. 64–69.
8. F.J. Humphreys: *J. Mater. Sci.*, 2001, vol. 36, pp. 3833–54.

9. O.V. Mishin, A. Godfrey, and L. Ostensson: *Metall. Mater. Trans. A*, 2006, vol. 37A, pp. 489–96.
10. G.L. Wu and D. Juul Jensen: *Mater. Charact.*, 2008, vol. 59, pp. 794–800.
11. A. Godfrey, N. Hansen, and D. Juul Jensen: *Metall. Mater. Trans. A*, 2007, vol. 38A, pp. 2329–39.
12. A. Godfrey, W.Q. Cao, N. Hansen, and Q. Liu: *Metall. Mater. Trans. A*, 2005, vol. 36A, pp. 2371–78.
13. W.T. Read and W. Shockley: *Phys. Rev.*, 1950, vol. 78, pp. 275–89.
14. W.T. Read: *Dislocation in Solids*, McGraw-Hill, New York, 1953, pp. 155–72.
15. F.J. Humphreys and M. Hatherly: *Recrystallization and Related Annealing Phenomena*, Elsevier, Oxford, 2004.
16. Y.B. Zhang, A. Godfrey, Q. Liu, W. Liu, and D. Juul Jensen: *Acta Mater.*, 2009, vol. 57, pp. 2631–39.
17. J.O. Stiegler, C.K.H. Dubose, R.E. Reed, and C.J. McHargue: *Acta Metall.*, 1963, vol. 11, pp. 851–60.
18. R.A. Vandermeer and W.B. Snyder, Jr: *Metall. Trans. A*, 1979, vol. 10, pp. 1031–44.
19. K. Verbeken, L. Kestens, and M.D. Nave: *Acta Mater.*, 2005, vol. 53, pp. 2675–82.
20. M. Sánchez-Araiza, S. Godet, P.J. Jacques, and J.J. Jonas: *Acta Mater.*, 2006, vol. 54, pp. 3085–93.
21. F. Huang, N.R. Tao, and K. Lu: *J. Mater. Sci. Technol.*, 2011, vol. 27, pp. 1–7.
22. Z.P. Luo, O.V. Mishin, Y.B. Zhang, H.W. Zhang, and K. Lu: *Scr. Mater.*, 2012, vol. 66, pp. 335–38.
23. J.M. Rosenberg and H.R. Piehler: *Metall. Trans.*, 1971, vol. 2, pp. 257–59.
24. Q. Xing, X. Huang, and N. Hansen: *Metall. Mater. Trans. A*, 2006, vol. 37A, pp. 1311–22.
25. I.L. Dillamore, C.J.E. Smith, and T.W. Watson: *Met. Sci.*, 1967, vol. 1, pp. 49–54.
26. W.B. Hutchinson and L. Ryde: in *16th Risø International Symposium Materials Science*, N. Hansen, D. Juul Jensen, Y.L. Liu, and B. Ralph, eds., Risø National Lab, Roskilde, 1995, p. 105.
27. I. Samajdar, B. Verlinden, P. Van Houtte, and D. Vanderschueren: *Mater. Sci. Eng. A*, 1997, vol. 238, pp. 343–50.
28. J.T. Park and J.A. Szpunar: *Acta Mater.*, 2003, vol. 51, pp. 3037–51.
29. R.L. Every and M. Hatherly: *Texture*, 1974, vol. 1, pp. 183–94.
30. W.B. Hutchinson: *Int. Met. Rev.*, 1984, vol. 29, pp. 25–42.
31. D. Raabe: in *16th Risø International Symposium Materials Science*, N. Hansen, D. Juul Jensen, Y.L. Liu, and B. Ralph, eds., Risø National Lab, Roskilde, 1995.
32. D. Raabe: *Steel Res.*, 1995, vol. 66, pp. 222–29.
33. M. Oyarzábal, A. Martínez-De-Guerenu, and I. Gutiérrez: *Mater. Sci. Eng. A*, 2008, vol. 485, pp. 200–09.
34. R. Khatirkar, B. Vadavadagi, S.K. Shekhawat, A. Haldar, and I. Samajdar: *ISIJ Int.*, 2012, vol. 52, pp. 884–93.
35. A.A. Gazder, M. Sánchez-Araiza, J.J. Jonas, and E.V. Pereloma: *Acta Mater.*, 2011, vol. 59, pp. 4847–65.
36. D. Juul Jensen: *Scr. Metall. Mater.*, 1992, vol. 27, pp. 533–38.